# Broadband Photoresponse Enhancement of a High-Performance *t*-Se Microtube Photodetector by Plasmonic Metallic Nanoparticles

*Kai Hu, Hongyu Chen, Mingming Jiang, Feng Teng, Lingxia Zheng, and Xiaosheng Fang**

**Broadband responsivity enhancement of single Se microtube (Se-MT) photodetectors in the UV–visible region is presented in this research. The pristine Se-MT photodetector demonstrates broadband photoresponse from 300 to 700 nm with peak responsivity of ≈19 mA $W^{-1}$ at 610 nm and fast speed (rise time 0.32 ms and fall time 23.02 ms). To further enhance the responsivity of the single Se-MT photodetector, Au and Pt nanoparticles (NPs) are sputtered on these devices. In contrast to only enhancement of responsivity in UV region by Pt NPs, broadband responsivity enhancement (≈600% to ≈800%) of the Se-MT photodetector is realized from 300 to 700 nm by tuning the size and density of Au NPs. The broadband responsivity enhancement phenomena are interpreted by both the surface modification and surface plasmon coupling. The experimental results of this work provide an additional opportunity for fabricating high-performance UV–visible broadband photodetectors.**

## 1. Introduction

Photodetectors with the ability to convert light (UV, visible, or infrared) into electric signal are fundamental to human life and have various applications including environmental monitoring, video-recording, ozone sensing, and optical communication.[1–5] In terms of the operation wavelength range, they are generally categorized into two types: special wavelength photodetectors and broadband photodetectors.[6] Special wavelength photodetectors response to certain narrow range of wavelength,[7] such as a solar-blind photodetector that operates from 220 to 280 nm[8] and an even photodetector with an enhanced UV photoresponse in a narrow spectrum range of only 17 nm.[9] In contrast to special wavelength photodetectors, broadband photodetectors response to wide range of light and satisfy the requirements of broadband light communication, imaging sensing, etc.[10,11] In particular, UV–visible photodetectors are one type of important broadband photodetectors that detect light from UV to visible range through the use of a single detector. To realize UV–visible light detection, materials with photoresponse in this broadband region are necessary. Silicon is the most widely used material among semiconductor materials as broadband photodetectors via metal–oxide–semiconductor (MOS) structure for its compatibility with current semiconductor industry. Nevertheless, a very thin oxide layer can cause large leakage current and a premature voltage broken down.[12] Hence, some other materials for UV–visible light detection are explored such as $MoS_2$, CdSe, $In_2Se_3$, and organic perovskites.[13–16] However, photodetectors based on these materials usually suffer seriously from instability, which impedes their wider application. Therefore, new strategies for high-performance broadband UV–visible light detection are necessary.

As a promising candidate for fabricating a high-performance broadband photodetector, p-type semiconductor Se exhibits many excellent properties.[17] For example, the band gap of Se is about 1.67 eV,[18] which means that Se exhibits broadband photoresponse from visible to UV region. Previous works also demonstrate that the conductivity of Se can rise from $10^{-6}$ to $10^{-5}$ $\Omega^{-1}$ $cm^{-1}$ to 0.59 $\Omega^{-1}$ $cm^{-1}$ under ≈$10^{-4}$ μW $\mu m^{-2}$ 633 nm laser illumination.[19,20] Furthermore, the response time of elemental selenium is very fast. The response time of amorphous Se film or Se nanobelts metal–semiconductor–metal (MSM) photodetector reaches several milliseconds,[18,21] much higher than ZnO, ZnS, and $MoS_2$ with a similar MSM structure.[13,22,23] Se microstructures synthesized by vapor phase deposition attract many interests for low cost, good crystallization, easy to build device, fast response, and also broadband photoresponse. In spite of these advantages, the responsivity of Se microstructure photodetectors is still lower than expected.

Recently, with the unique ability to route and manipulate light at nanoscale beyond the diffraction limit, surface plasmon resonance arising from metallic nanoparticles (NPs) offers new opportunities to improve the performance of optoelectronic devices.[24,25] Up to now, it has demonstrated significant potential

K. Hu, Dr. H. Y. Chen, Dr. F. Teng, Dr. L. X. Zheng, Prof. X. S. Fang
Department of Materials Science
Fudan University
Shanghai 200433, P. R. China
E-mail: xshfang@fudan.edu.cn
Dr. M. M. Jiang
State Key Laboratory of Luminescence and Applications
Changchun Institute of Optics
Fine Mechanics and Physics
Chinese Academy of Sciences
Changchun 130033, P. R. China

DOI: 10.1002/adfm.201602408

for improving the performance of light-emitting diodes, lasers, solar cells, and especially responsivity of photodetectors.[26,27] The additional tremendous local electromagnetic fields are attributed to the redistributing surface charges of metallic NPs. And their surface charges can be modified by changing shapes, distances, and materials of metallic NPs. This allows one to tailor the surface plasmon resonance frequency and manipulate scattering from the NPs over a broad wavelength range.[28,29] Even so, recent researches mainly focus on the selective enhancement photodetection of surface plasmon in a narrow wavelength range.[30,31] Concerning the UV to visible photoresponse of Se semiconductor, broadband enhancement in UV–visible region is needed.

In this paper, Se microtubes (Se-MTs) are successfully prepared via a facile vapor transport and deposition route. After that, a single Se-MT is constructed into photodetector device using indium as electrodes. Broadband (300–700 nm) and fast (rise time of 0.32 ms and fall time of 23.02 ms) photoresponses are realized by the Se-MT with peak responsivity of ≈19 mA $W^{-1}$ at 610 nm. The photoresponse enhancement effect of Pt and Au NPs on single Se-MT photodetectors is studied and it demonstrates that broadband enhancement of responsivity has been realized by Au nanoparticles, while only UV range (300–400 nm) enhancement has been found by Pt NPs. The results show that by coupling plasmonic Au NPs on surface of Se-MT photodetectors, ≈600% to ≈800% improvement of responsivity is realized in wideband range (≈300 to ≈700 nm). To get insight into the enhancement mechanism, theoretical analysis in conjunction with finite difference time-domain (FDTD) method is also performed in the following. The method of fabricating single Se-MT-based photodetector and its broadband responsivity enhancement by Au NPs is expected to apply to UV–visible light detection.

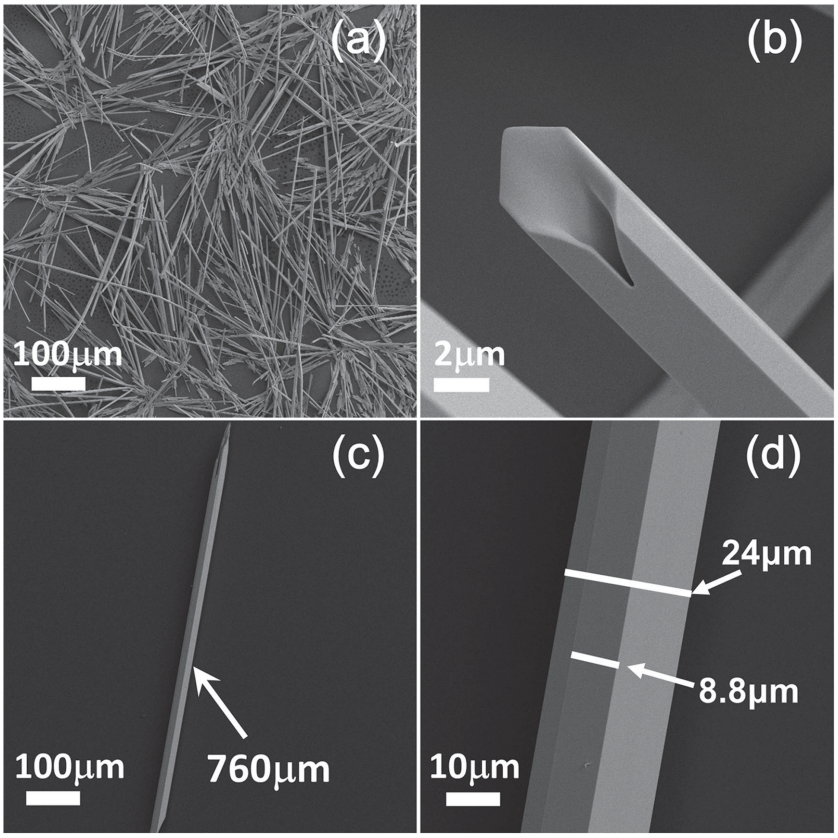


**Figure 1.** SEM images of Se-MTs. a,b) Low and high magnification SEM images of as-grown Se-MTs on $Si/SiO_2$ wafer. c,d) A typical single Se-MT.

## 2. Results and Discussion

**Figure 1** shows the field-emission scanning electron microscopy (FESEM) characterization of as prepared Se-MTs with a large scale. The width of Se tubes varies from several micrometers to tens of micrometers and the length of Se-MTs can reach several millimeters as depicted in Figure 1a. The magnified image in Figure 1b reveals that Se-MTs are in hexagon shape with a hollow tubular morphology. Figure 1c,d shows a typical single Se-MT with a length of 760 μm, a uniform width of 24 μm along the whole single microtube and one edge length of the tube of 8.8 μm. The phases of as prepared tubes are further confirmed by X-ray diffraction (XRD) patterns as shown in **Figure 2**a. The sharp diffraction peaks demonstrate good crystallinity of Se-MTs. All diffraction peaks can be assigned to trigonal selenium (*t*-Se, JCPDS No. 65-1876) with the lattice parameters of $a = b = 4.364$ Å, $c = 4.959$ Å. Figure 2b presents the UV–visible absorption and reflection spectra within 350–700 nm range of as prepared *t*-Se MTs, which are vital to study the photoelectric performance. The absorption of elemental selenium increases dramatically from nearly zero to a maximum value of ≈1.0 from 650 to 550 nm and then stays steady afterward. While the reflection drops accordingly from ≈80% to ≈55% between 650 and 550 nm and then slowly decreases to ≈40% (350 nm). It is noteworthy that the Se-MTs exhibit both UV and visible light response with a cutoff wavelength estimated to be ≈660 nm.

Because the as fabricated Se-MTs are thick and long enough to be visible to the eyes, a single Se-MT is easily transferred to glass substrate and indium electrodes are then manually patterned on both sides of the microtube for device construction as schematic illustration in **Figure 3**a. The light active area is estimated to be $2.4 \times 10^{-8}$ $m^2$. Incident light irradiates the device vertically. Figure 3b shows the current–voltage (*I–V*) characteristics of the single Se-MT photodetector in dark, 350, 450, and 610 nm light illumination in semilogarithmic coordinates. *I–V* characterization in linear coordinates is also given in the inset of Figure 3b. Linear *I–V* characteristic of the device reveals the Ohmic contact between Se-MT and indium electrodes. It shows that the device exhibits excellent photoresponse under 610 nm (0.434 mW $cm^{-2}$), 450 nm (1.003 mW $cm^{-2}$),

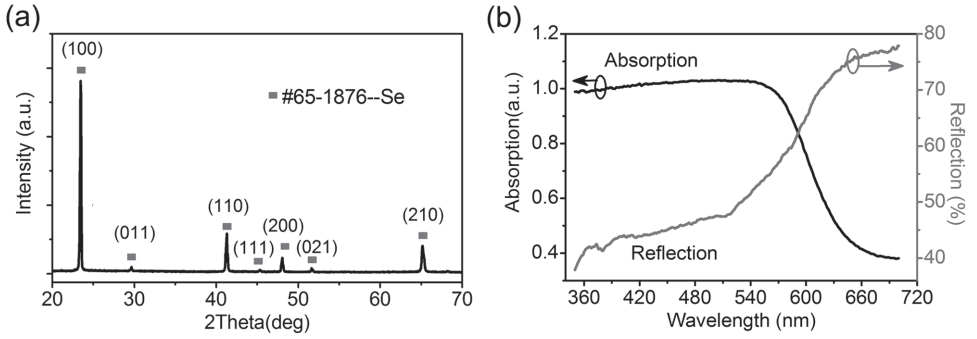


**Figure 2.** a) XRD pattern of as grown Se-MTs. b) UV–visible absorption and reflection spectra of elemental *t*-Se.

and 350 nm (0.753 mW cm$^{-2}$) irradiation. This means that the device exhibits broadband light response from UV to red visible light range. This is further confirmed by its spectral responsivity at 5 V bias recorded from 300 to 700 nm (Figure 3c).

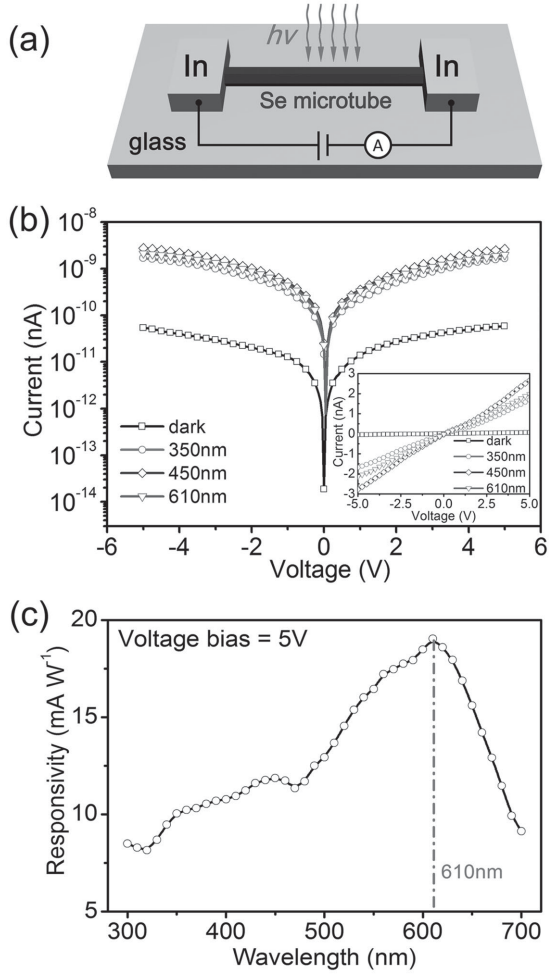


**Figure 3.** Photoelectric performance of single Se-MT photodetector. a) Schematic diagram of a single Se-MT photodetector. b) *I–V* characteristics of the photodetector under dark and illumination with 610 nm red light (0.434 mW cm$^{-2}$), 450 nm (1.003 mW cm$^{-2}$), and 350 nm UV light (0.753 mW cm$^{-2}$). c) Spectral response of the single Se-MT device at 5 V bias.

The responsivity $R_\lambda$ is calculated according to the following equation[32,33]

$$R_\lambda = \left(I_{\text{light}} - I_{\text{dark}}\right)/P_\lambda S \tag{1}$$

where light current $I_{\text{light}}$, dark current $I_{\text{dark}}$, light power density $P_\lambda$, and effective illuminated area $S$ are available from measured data. It is obvious that the Se-MT device shows broadband photoresponse with a highest peak responsivity of ≈19 mA W$^{-1}$ at 610 nm and two small peaks located at 450 and 350 nm. The responsivity decreases sharply after 610 nm, showing its spectral cutoff characteristic. The cutoff wavelength is estimated to be ≈670 nm, which agrees quite well with the UV–visible absorption and reflection spectra of elemental Se (Figure 2b).

Additionally, the stability and sensitivity are also critical to examine the performance of photodetector devices. **Figure 4**a shows the current–time (*I–t*) curve of the single Se-MT device under three different light wavelengths illumination at 5 V bias, which indicates good stability and reversibility without notable photocurrent decay. The current increases quickly to a stable value upon light illumination and then decays dramatically to the original value when the light switched off. It indicates that the device is very stable under periodic light illumination and also has very short response time. The photocurrents are found to be 1.66, 2.53, and 1.78 nA under 350 nm (0.753 mW cm$^{-2}$), 450 nm (1.003 mW cm$^{-2}$), and 610 nm (0.434 mW cm$^{-2}$) periodical light irradiation, respectively. Although the highest photocurrent is under 450 nm light illumination, the largest responsivity is located at 610 nm (Figure 3c) attributing to the much lower light power density of 610 nm according to Equation (1). The dark current of the Se-MT photodetector is about 60 pA as seen in Figure S1 (Supporting Information). The on/off ratio $(I_{\text{light}} - I_{\text{dark}})/I_{\text{dark}}$ of this device under 350, 450, and 610 nm is 27, 45, and 32, respectively. To better illustrate the time resolved property of the device, a quick response measure system (experimental setup is shown in the inset of Figure 4b) is applied and pulse response of single Se-MT device is given in Figure 4b,c. The quick response measure system uses a pulsed YAG:Nd laser as a light source, the voltage of series resistor as a function of time is recorded by the oscilloscope. When the pulse laser irradiates the photodetector, the resistance of sample decreases, leading to the rising of partial voltage on series resistor. The photoresponse of single Se-MT device is very fast, highly stable, and reproducible as displayed

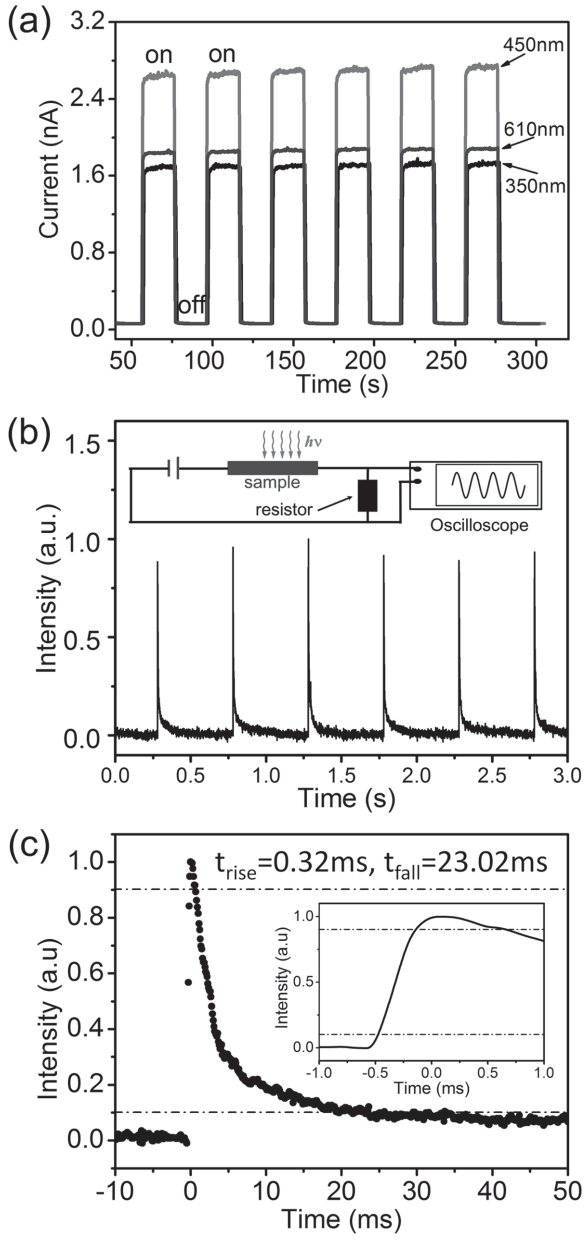


**Figure 4.** Current–time properties of single Se-MT photodetector. a) *I–t* characteristics with on/off switching upon 610, 450, and 350 nm light illumination under 5 V bias. b) Pulse response of Se-MT photodetector under 2 Hz 355 nm pulse laser radiation. Inset: Schematic diagram of quick response measure system. c) Single period of pulse response in (b). Inset: Rising edge of pulse response.

in Figure 4b. The fall time from 90% to 10% is ≈23.02 ms and rise time from 10% to 90% is ≈0.32 ms (inset in Figure 4c). From the above experimental results, it is obvious that the single Se-MT device shows broadband detectivity from UV to visible range, high stability and sensitivity, as well as fast response speed, but relatively low responsivity comparing to a conventional photodetector.[1,33]

To further improve the broadband responsivity, metallic NPs are then sputtered on the surface of Se-MT by a simple ion sputtering deposition method. SEM images of surface morphology

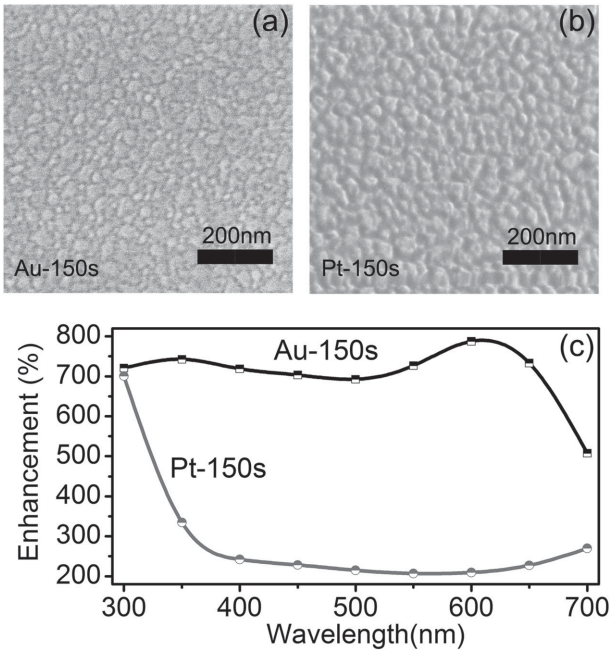


**Figure 5.** Surface plasmon enhancement detection by metal particles. a,b) SEM images of surface morphology of Se-MT sputtered Au and Pt with the same experimental conditions (sputtering time: 150 s). c) Spectral responsivity enhancement of Se-MT photodetector enhanced by Au and Pt NPs.

after sputtering Au and Pt are shown in **Figure 5**a,b, respectively. The sputtering time for both metals is 150 s. It can be seen that surface morphology varies when using different noble metals under the same condition. Both show good adhesion to Se-MTs with diameters between 10 and 50 nm, which is suitable for plasmonic resonance.[34] Similarly, both Au-Se and Pt-Se hybrid photodetector devices are constructed using indium as the electrodes and the spectral responsivities are measured. Figure 5c reveals the responsivity enhancement effect after sputtering metallic NPs comparing with pristine Se-MT devices. The responsivity enhancement is defined as $R_t/R_0$ where $R_t$ is the responsivity after sputtering metal for t(s) and $R_0$ is the responsivity without sputtering metallic nanoparticles. Interestingly, the responsivity enhancement of Au is much higher than that of Pt in visible region. For Pt NPs, the enhancement effect is low at visible light range and becomes very high in UV region, suggesting better UV selectivity, which can be explained by UV region plasmonic resonance of Pt NPs reported previously,[35] while Au NPs enable large responsivity enhancement (>500%) in both UV and visible range. The highest enhancement is nearly 800% under 600 nm incident light.

In order to get more insight into the enhancement effects of Au NPs and explore the mechanism of responsivity improvement, we systematically adjusted the size and distribution of Au NPs by simply tuning the sputtering time from 60 to 210 s. **Figure 6**a shows the spectral responsivity dependence of Au-Se-MT hybrid photodetectors on tailored Au NPs in different sputtering time. All the responsivity spectra for these devices demonstrate similar patterns as the one for single Se-MT photodetector in Figure 3c, revealing a similar spectral response property. Generally, when increasing sputtering time

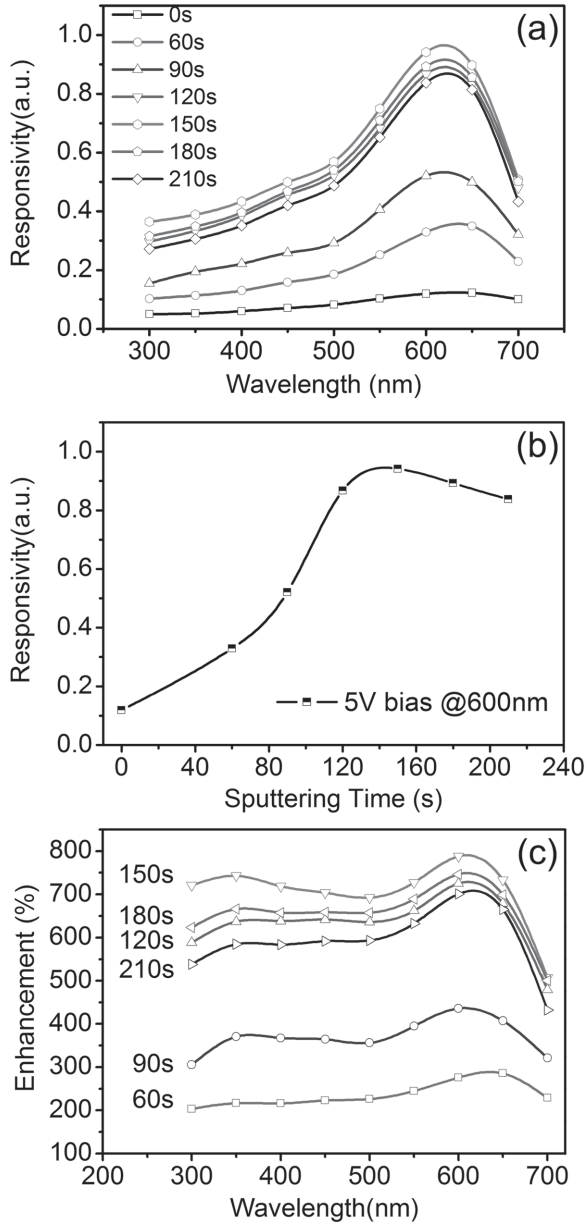


**Figure 6.** Photoresponse enhancement of single Se-MT photodetector by sputtered Au NPs. a) Spectral responsivity of single Se-MT photodetectors with various Au sputtering times under 2 mA current (bias = 5 V). b) Responsivity of Se photodetector as a function of sputtering time under 600 nm. c) Spectral enhancement of Se-MT photodetector by Au nanostructures.

from 60 to 210 s, the spectral responsivity within UV and visible range greatly increases, reaches a maximum at 150 s, and then drops slowly. The relationship between the responsivity at 600 nm and the sputtering time is outlined in Figure 6b. The rise–fall process of responsivity can be explained qualitatively according to SEM images (Figure S2, Supporting Information) of Au NPs prepared under different sputtering time. Initially, the Au NPs grow bigger and denser as the sputtering time increases, leading to stronger plasmonic resonance effect. However, when the sputtering process continues (i.e., >150 s in this study), Au NPs become so dense that they can block the light intake by Se, resulting in a decreasing responsivity. In addition, the spectral responsivity enhancement curves with tunable Au NPs in Figure 6c suggest excellent broadband (from 300 to ≈700 nm) enhancement effects caused by Au NPs. The highest enhancement reaches ≈800% when sputtering Au at 150 s at 600 nm compared to the original single Se-MT device, owing to the surface plasmon resonance excited by Au NPs.

As is aforementioned, the spectral response enhancement of Se-MT photodetectors is highly dependent on the kind of metallic NPs with the same density (see Figure 3). As for Pt samples, their enhancement ratios are relatively small in the wavelength range from 400 to 700 nm with weak wavelength dependence. Nevertheless, the tunable enhancement ratio could be tailored by controlling the sputtering time of Au NPs. These generating more electron–hole pairs may arise from the surface plasmon resonance effects of the Au NPs by the localized electric field enhancement effect and related scattering effect, because their minimal s–d interband transition rates are usually at energies below 2.4 eV.[36] To confirm the above hypothesis and shed light on the origin of plasmon resonance between the Au NPs and Se-MT, the extinction spectra (scattering + absorption) of Au NPs were simulated via the FDTD method based on the optical constants measured by Johnson and Christy.[37] In the following simulations, Se-MT was considered in our calculations.

As is well known, the spectral shape and position of the surface plasmon resonances in the metallic NPs are highly sensitive to their size, shape, and internal gap.[28,38] To simplify the models, the extinction spectra of isolated Au nanosphere based on our experiment (**Figure 7**a) are calculated. As is shown in Figure 7b, with increasing the size of NPs, the plasmon resonance redshifts, and all peak wavelength of extinction for isolated Au NPs ranging from 10 to 50 nm mainly locates from ≈550 to ≈650 nm. According to the simulation, the spectral position of the plasmon resonance for an Au NP with a diameter of 50 nm is the nearest to the response peak wavelength of Se-MT photodetectors (610 nm), which somewhat deviates from the experimental results (Figure 7a: Au NPs with 35 nm diameter are major). Herein, considering the random dispersion of Au NPs in our experiment, the interaction among the NPs could not be ignored, which would affect the resonance position of surface plasmon in a way. In Figure 7c, the extinction spectra of the dimer with a nanosphere (diameter $d = 35$ nm) with various interspace gaps ($g = 10$–$50$ nm) are carried out. With decreasing $g$, the plasmon resonance redshifts. It indicates that surface plasmon resonances located around 600 nm can be obtained when interspace gap between two NPs is smaller than 30 nm. In our experiment, the major interspace gap ($g$) between two NPs is around 15 nm. To account for these features of our experiments, $g$ is fixed at 15 nm, and simulations of Au dimers with different NPs size were performed and shown in Figure 7d. In addition to appearance of multipolar resonance,[39] similar to the isolated Au NPs, with the increase in $d$ of the NPs in dimer, their resonance peaks shift to longer wavelengths, and those located around 600 nm can be obtained when the size of NPs is around 35 nm. Therefore, it could be confirmed that the spectral response enhancement near absorption edge of Se is mainly arising from the surface plasmon resonance in our experiment.

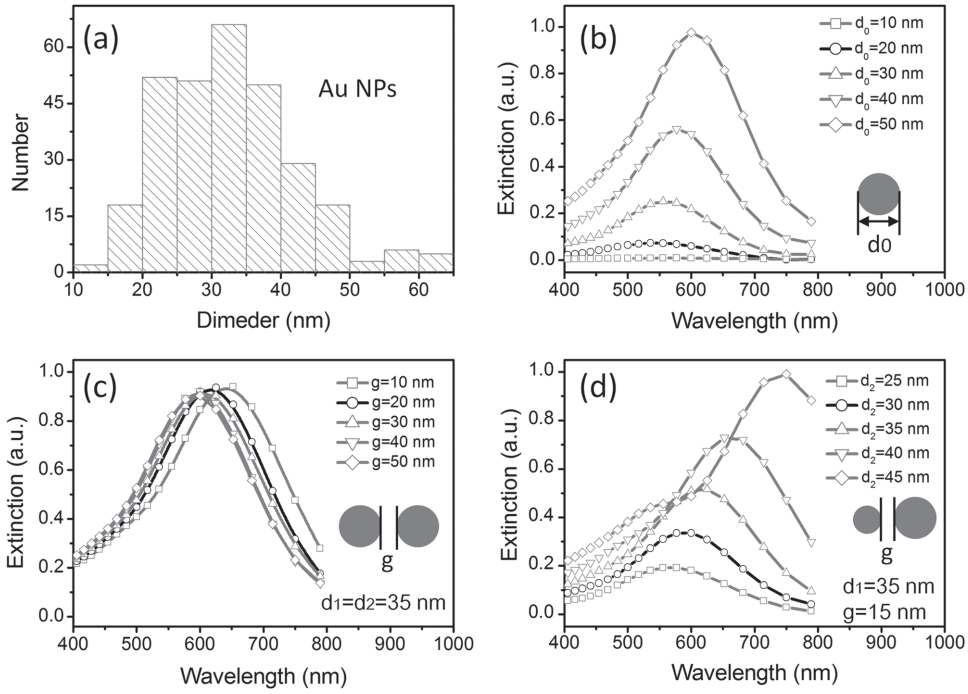


**Figure 7.** a) The size distribution of Au NPs with the sputtering time at 150 s. b–d) Extinction spectra, and the spatial distribution of the electric field obtained by FDTD simulation. b) Extinction spectra of the isolated nanospheres with $d_0$ = 10, 20, 30, 40, and 50 nm. c) Dimer consists of two nanospheres ($d$ = 35 nm) with the interspace gap of 10–50 nm. d) Extinction spectra of the dimer with one nanosphere diameter $d_1$ = 25, 30, 35, 40, and 45 nm. Another nanosphere diameter $d_1$ and the internal gap g are fixed at 35 and 15 nm, respectively.

In addition, the electric field distributions of Au NPs (**Figure 8**) demonstrate that the intensity of surface plasmon resonance is highly sensitive to the coupling of Au NPs. Compared with the single Au NP, the incident light could be much easier to be constricted and penetrated into the active region of Se-MT photodetector. This additional energy would play an important role in the separation of photon-generated carriers.

In the process of above simulations, albeit it cannot completely exclude the contribution of the interaction between the dimers, the random Au NPs were qualitatively recognized as the collection of the dimers. The experiment results (Figures 5 and 6) can be well explained by the simulation results in the visible range, especially the relatively higher enhancement of photodetection at the wavelength around 600 nm. Moreover, integrated by charge transition and scattering effect of the metallic NPs, the broad enhancement of Se-MT photodetectors can be actively controlled in a broad wavelength range by tuning the interspace gap and density of Au NPs, which could in turn modulate the absorption and release energy of Au NPs. In contrast, owning to the surface plasmon properties of Pt, only a much narrower band enhancement in the UV range can be observed for Pt samples.[35,40] In addition, work function of Pt (5.65 eV) is larger than that of Au (5.1 eV); the additional energy difference would suppress the charge transfer.[41] In addition to the contribution of surface plasmon resonance to the responsivity enhancement, the unique pattern of the Au NPs can also

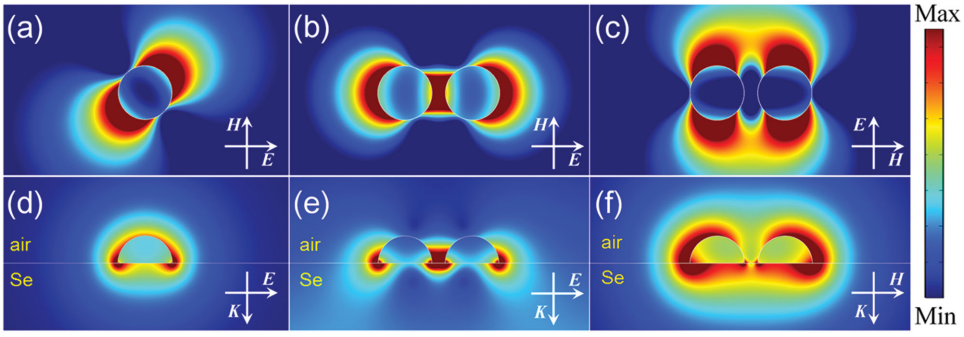


**Figure 8.** Spatial distribution of the electric field intensity at the wavelength of 600 nm. (a)–(c) are perpendicular to the direction of incident light; (d)–(f) are parallel to the direction of incident light. The diameter of Au NPs is 40 nm and the interspace gap of dimer is 10 nm.

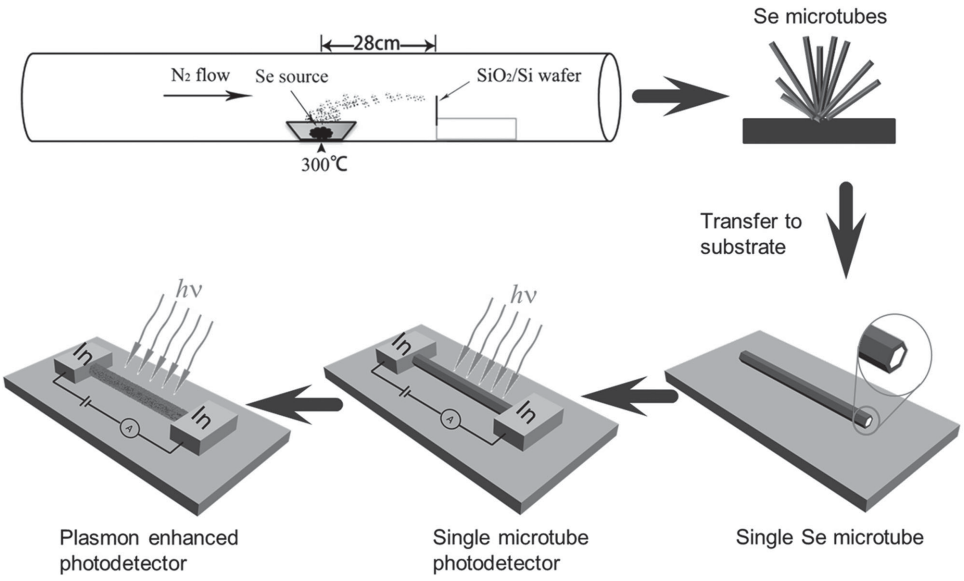


**Scheme 1.** Schematic illustration of Se-MT fabrication and device construction.

contribute a lot to responsivity enhancement over broadband region, especially in the UV region as reported previously.[25,42] Hence, the very weak enhancement in the visible range would be mainly attributed to the scattering effect of the metal NPs.

## 3. Conclusion

Broadband photodetector from UV to visible is presented based on single Se-MT. The photodetector exhibits broadband UV–visible photoresponse, excellent photosensitivity, stability, and fast speed (0.32 ms/23.02 ms). Moreover, 600%–800% improvement of responsivity is realized in wideband range (from ≈300 to ≈700 nm) by sputtering Au NPs, which is then further studied via FDTD simulation. The broadband responsivity enhancement phenomena are interpreted by both the surface modification and surface plasmon coupling. The single Se-MT is expected to be a promising candidate of fabricating a UV–visible broadband photodetector. Furthermore, the broadband enhancement in responsivity achieved by Au NPs in this work is also a promising pathway to improve photoresponse of other UV–visible photodetectors.

## 4. Experimental Section

*Synthesis of Se-MTs*: The synthesis of Se-MTs was carried out in a horizontal tube furnace via vapor transport and deposition process. Se source (>99.95%, Meixing Chemical Co., LTD, Shanghai) was in the center of the furnace and silicon wafer was placed 28 cm downstream from the center vertically. Before heating, ultrapure nitrogen was flushed at rate of 400 standard cubic center meter (sccm) for nearly 30 min to remove residual air. Then, the center temperature of the tube furnace was heated to 300 °C in 55 min and was maintained at 300 °C for 720 min with a constant nitrogen flow of 300 sccm. The temperature at the silicon wafer was about 150 °C during the growth process. The growth of Se-MTs was carried out on a cleaned $Si/SiO_2$ wafer.

*Device Fabrication*: The synthesized MTs were then transferred to glass without further treatment. The MSM structure photodetector was then constructed using indium electrodes on both sides of a single Se-MT. Metallic NPs were fabricated by ion sputtering equipment (Hetongchuangye Co., Ltd, Beijing) with selectable Au and Pt target materials. The as constructed MSM device was put on the chamber of the equipment which was then vacuumed to 0.15 mbar. The sputtering process was carried out under the condition of 2 mA sputtering current and time varying from 60 to 210 s. After sputtering, the device was then heated for 3 min at 90 °C. Finally, the device was naturally cooled down to room temperature. For the measurement of responsivity enhancement, one MSM device was sputtered repeatedly to ensure the comparability. The above procedures are schematically illustrated in **Scheme 1**.

*Material Characterization*: Morphology of as synthesized Se microstructure materials was characterized by FESEM (Zeiss Sigma) and phase of the material was further identified by XRD (Bruker D8-A25) using Cu$K\alpha$ radiation ($\lambda$ = 0.15406 nm) in the $2\theta$ range from 20° to 65°. The optical properties of elemental Se were characterized using a UV–visible spectrophotometer (Hitachi U-3900H).

*Photoelectric Measurements*: The photoelectric properties (*I–V* and *I–t* characteristics) and spectral photoresponses of the photodetectors were characterized by a semiconductor characterization system (Keithley 4200-SCS), a 24 W Xe lamp (POWERMAX II P21NRX3), and monochromators. Time resolved responses of the device were measured via the circuit in the inset of Figure 4b with YAG:Nd laser with pulse duration of 3–5 ns (Continuum Electro-Optics, MINILITE II, 355 nm), oscilloscope (Tektronix MSO/DPO5000), and a 1 GΩ resistor.

## Supporting Information

Supporting Information is available from the Wiley Online Library or from the author.

## Acknowledgements

K.H. and H.Y.C. contributed equally to this work. This work was supported by the National Natural Science Foundation of China (Grant Nos. 51471051, 11404328, 61505033, and 11574307), the National

Postdoctoral Science Foundation of China (Grant No. 2015M580294), the Science and Technology Commission of Shanghai Municipality (Grant Nos. 15520720700 and 13NM1400300), Shanghai Shu Guang Project (Grant No. 12SG01), and the Programs for Professor of Special Appointment (Eastern Scholar) at Shanghai Institutions of Higher Learning. Part of this work was carried out in Fudan Nano-fab Laboratory.

Received: May 16, 2016
Revised: June 24, 2016
Published online: July 21, 2016

[1] G. Konstantatos, E. H. Sargent, *Nat. Nanotechnol.* **2010**, *5*, 391.
[2] H. Y. Chen, H. Liu, Z. M. Zhang, K. Hu, X. S. Fang, *Adv. Mater.* **2016**, *28*, 403.
[3] H. Lu, W. Tian, F. R. Cao, Y. L. Ma, B. K. Gu, L. Li, *Adv. Funct. Mater.* **2016**, *26*, 1296.
[4] X. S. Fang, L. F. Hu, K. F. Huo, B. Gao, L. J. Zhao, M. Y. Liao, P. K. Chu, Y. Bando, D. Golberg, *Adv. Funct. Mater.* **2011**, *21*, 3907.
[5] H. Y. Chen, K. W. Liu, L. F. Hu, A. A. Al-Ghamdi, X. S. Fang, *Mater. Today* **2015**, *18*, 493.
[6] X. Hu, X. Zhang, L. Liang, J. Bao, S. Li, W. Yang, Y. Xie, *Adv. Funct. Mater.* **2014**, *24*, 7373.
[7] Q. Lin, A. Armin, P. L. Burn, P. Meredith, *Nat. Photonics* **2015**, *9*, 687.
[8] L. Peng, L. F. Hu, X. S. Fang, *Adv. Mater.* **2013**, *25*, 5321.
[9] H. Zhu, C. Shan, B. Yao, B. Li, J. Zhang, D. Zhao, D. Shen, X. Fan, *J. Phys. Chem. C* **2008**, *112*, 20546.
[10] C. H. Liu, Y. C. Chang, T. B. Norris, Z. H. Zhong, *Nat. Nanotechnol.* **2014**, *9*, 273.
[11] L. Menon, H. Yang, S. Cho, S. Mikael, Z. Ma, C. Reuterskiöld-Hedlund, M. Hammar, W. Zhou, *IEEE Photonics J.* **2016**, *8*, 1.
[12] Z. Yu, M. Aceves-Mijares, *Appl. Phys. Lett.* **2009**, *95*, 081101.
[13] O. Lopez-Sanchez, D. Lembke, M. Kayci, A. Radenovic, A. Kis, *Nat. Nanotechnol.* **2013**, *8*, 497.
[14] Y. Guo, C. Liu, H. Tanaka, E. Nakamura, *J. Phys. Chem. Lett.* **2015**, *6*, 535.
[15] T. Y. Zhai, X. S. Fang, M. Y. Liao, X. Xu, L. Li, B. Liu, Y. Koide, Y. Ma, J. N. Yao, Y. Bando, *ACS Nano* **2010**, *4*, 1596.
[16] Y. Jiang, W. J. Zhang, J. S. Jie, X. M. Meng, X. Fan, S. T. Lee, *Adv. Funct. Mater.* **2007**, *17*, 1795.
[17] J. Mort, *Phys. Rev. Lett.* **1967**, *18*, 540.
[18] L. B. Luo, X. B. Yang, F. X. Liang, J. S. Jie, Q. Li, Z. F. Zhu, C. Y. Wu, Y. Q. Yu, L. Wang, *CrystEngComm* **2012**, *14*, 1942.
[19] P. Liu, Y. Ma, W. Cai, Z. Wang, J. Wang, L. Qi, D. Chen, *Nanotechnology* **2007**, *18*, 205704.
[20] K. Murphy, B. Wunderlich, B. Wunderlich, *J. Phys. Chem.* **1982**, *86*, 2827.
[21] W. Kai, C. Feng, G. Belev, S. Kasap, K. S. Karim, *Appl. Phys. Lett.* **2009**, *95*, 013505.
[22] H. Kind, H. Yan, B. Messer, M. Law, P. D. Yang, *Adv. Mater.* **2002**, *14*, 158.
[23] X. S. Fang, Y. Bando, M. Y. Liao, U. K. Gautam, C. Y. Zhi, B. Dierre, B. D. Liu, T. Y. Zhai, T. Sekiguchi, Y. Koide, D. Golberg, *Adv. Mater.* **2009**, *21*, 2034.
[24] J. A. Schuller, E. S. Barnard, W. Cai, Y. C. Jun, J. S. White, M. L. Brongersma, *Nat. Mater.* **2010**, *9*, 193.
[25] E. R. Martins, J. Li, Y. Liu, V. Depauw, Z. Chen, J. Zhou, T. F. Krauss, *Nat. Commun.* **2013**, *4*, 2665.
[26] M. M. Jiang, B. Zhao, D. Zhao, D. Shen, F. Wang, Y. Li, *Nanoscale* **2014**, *7*, 1081.
[27] H. A. Atwater, A. Polman, *Nat. Mater.* **2010**, *9*, 205.
[28] C. L. Nehl, J. H. Hafner, *J. Mater. Chem.* **2008**, *18*, 2415.
[29] K. M. Mayer, J. H. Hafner, *Chem. Rev.* **2011**, *111*, 3828.
[30] C. C. Chang, Y. D. Sharma, Y. S. Kim, J. A. Bur, R. V. Shenoi, S. Krishna, D. Huang, S. Y. Lin, *Nano Lett.* **2010**, *10*, 1704.
[31] Y. Liu, R. Cheng, L. Liao, H. Zhou, J. Bai, G. Liu, L. Liu, Y. Huang, X. F. Duan, *Nat. Commun.* **2011**, *2*, 579.
[32] H. Liu, Z. M. Zhang, L. F. Hu, N. Gao, L. W. Sang, M. Y. Liao, R. Z. Ma, F. F. Xu, X. S. Fang, *Adv. Opt. Mater.* **2014**, *2*, 771.
[33] B. Zhao, F. Wang, H. Y. Chen, Y. Wang, M. M. Jiang, X. S. Fang, D. X. Zhao, *Nano Lett.* **2015**, *15*, 3988.
[34] S. Link, M. A. El-Sayed, *J. Phys. Chem. B* **1999**, *103*, 4212.
[35] C. Tian, D. Jiang, J. Pei, L. Sun, R. Liu, Z. Guo, J. Hou, J. Zhao, Q. Liang, S. Gao, *J. Alloys Compd.* **2016**, *667*, 65.
[36] B. J. Lawrie, K. W. Kim, D. P. Norton, R. F. Haglund Jr., *Nano Lett.* **2012**, *12*, 6152.
[37] P. B. Johnson, R. W. Christy, *Phys. Rev. B* **1972**, *6*, 4370.
[38] S. Linic, P. Christopher, D. B. Ingram, *Nat. Mater.* **2011**, *10*, 911.
[39] H. Y. Chen, K. W. Liu, M. M. Jiang, Z. Zhang, X. Xie, D. Wang, L. Liu, B. Li, D. Zhao, C. Shan, *Appl. Phys. Lett.* **2014**, *104*, 091119.
[40] J. M. Lin, H. Y. Lin, C. L. Cheng, Y. F. Chen, *Nanotechnology* **2006**, *17*, 4391.
[41] V. Subramanian, E. E. Wolf, P. V. Kamat, *J. Phys. Chem. B* **2003**, *107*, 7479.
[42] A. J. Smith, C. Wang, D. Guo, C. Sun, J. Huang, *Nat. Commun.* **2014**, *5*, 5517.